Correlated displacement of dynamic elastic dipoles produces non-classical electrostriction in Zr-doped

ceria

Tali Pechersky-Savich^{1, ‡}, Boyuan Xu^{2, ‡}, Maxim Varenik^{1, ‡}, Junying Li³, Ellen Wachtel¹, David Ehre¹, Prahlad K. Routh³, Nicholas Marcella⁴, Anatoly I. Frenkel^{3, 5*}, Yue Qi^{6,*}, Igor Lubomirsky^{1,*}

¹ Department of Molecular Chemistry and Materials Science, Weizmann Institute of Science,
Rehovot, 7610001, Israel

Department of Physics, Brown University, Providence, RI 02912, USA
 Department of Materials Science and Chemical Engineering, Stony Brook University, Stony

Brook, NY 11794, USA

⁴ Department of Chemistry, University of Illinois, Urbana, IL, 61801, USA

⁵ Division of Chemistry, Brookhaven National Laboratory, Upton, NY 11973, USA

⁶ School of Engineering, Brown University, Providence, RI 02912, USA

[‡]These authors contributed equally: Tali Pechersky-Savich, Maxim Varenik, Boyuan Xu.

*Email:anatoly.frenkel@stonybrook.edu; yueqi@brown.edu; igor.lubomirsky@weizmann.ac.il

Abstract

By combining experimental data with density functional theory-based *ab initio* molecular dynamics modeling, this work provides evidence that non-classical electrostriction in isovalent Zrdoped ceria is due to the correlated anharmonic motion of dynamic elastic dipoles associated with multiple [ZrO₈]-local bonding units with high Zr concentration (Zr_{0.1}Ce_{0.9}O₂). Introduction of 0.5

mol% trivalent or divalent co-dopants (Sc, Yb, La or Ca) reduces the longitudinal electrostriction strain coefficient by more than a factor of ten, produces a threefold decrease in the relative dielectric permittivity, and increases the elastic modulus. Since these changes depend neither on the crystal radius nor valency of the co-dopant, we conclude that the responsible species are charge-compensating oxygen vacancies (Vo). For trivalent dopants (Do0.005Zr0.1Ce0.895O1.9975), oxygen vacancies are present at a concentration ratio 1:40 with respect to Zr, giving, for random distribution, a characteristic interaction distance \$2.3 unit cells (1.2 nm). Oxygen vacancies participate in [ZrO7-Vo] local bonding units, disrupting the correlated dynamic displacements of the connected [ZrO8]-local bonding units. Such correlated motion of dynamic elastic dipoles may also explain the exponential increase in the longitudinal electrostriction strain coefficient with increase in Zr-concentration to <0.2 mol fraction and must be taken into account for further development of non-classical electrostrictors based on Zr-doped ceria.

1 Introduction

Electrostriction is a second order electromechanical response: strain is proportional to the square of the electric field. Electrostriction is described by a fourth-rank tensor and is not restricted to a specific crystal symmetry, as is piezoelectricity. For most materials, the electrostriction polarization coefficient scales with the ratio of elastic compliance and dielectric permittivity (R. Newnham scaling law ^{1, 2}). This dependence is rooted in the anharmonicity of the interatomic bonds in the lattice, following the model of K. Uchino³. However, during the last decade, there have appeared literature reports on the observation of electrostriction in oxygen ion conductors^{2, 4-16} (aliovalent – doped ceria; Y-stabilized cubic zirconia) and proton conductors¹⁷. For these stiff, relatively low dielectric permittivity materials, the electrostriction polarization coefficient exceeds, by up to two orders of magnitude, that predicted by the classical scaling law¹. This enhanced effect, termed non-classical electrostriction (NCES), has been attributed to the presence of polarizable elastic dipoles associated with orientationally mobile point defects ^{2, 5, 6, 8-12, 15, 16, 18-23}.

We have recently reported on NCES observed in Zr doped ceria containing up to 10 mol% Zr $(10\text{ZDC})^{24}$. 10ZDC is not an ionic conductor in its oxidized state (< 100 ppm of Ce^{3+}). While 10ZDC contracts parallel to the direction of the electric field, as do electromechanically active aliovalent doped ceria films and ceramics^{4, 7, 8, 14}, the origin of NCES in 10ZDC must be fundamentally different from NCES in aliovalent, e.g., Sm- or Gd- doped ceria. The longitudinal electrostriction strain coefficient of 10ZDC, $M_{33} = -10^{-16} \, m^2/V^2$ remains essentially constant for frequency $f \leq 3.5 \, \text{kHz}$, falling by $\approx 50\%$ at $6.5 \, \text{kHz}^{24}$. This is indeed comparable in magnitude and frequency range to the best commercial electrostrictor, the relaxor ferroelectric 85 mol% $PbMg_{\frac{1}{3}}Nb_{\frac{2}{3}}O_3$ -15 mol% $PbTiO_3$ (PMN-PT15) ²⁵, for which M_{33} ranges between +2 to +4

·10⁻¹⁶ m^2/V^2 and for which the relaxation frequency lies between 6-10 kHz^{26, 27}. This is in contrast to Sm- or Gd- doped ceria (SmDC, GDC) for which M₃₃ is large and negative: M_{33} = $-(0.1 \text{ to } 1)10^{-16} m^2/V^2$, but which decays by approximately two orders of magnitude already at f=10 Hz. For 10ZDC, the linear relationship between strain and the square of the electric field amplitude persists to at least -220 ppm, which suggests that the saturation strain, i.e., the strain at which increasing the electric field no longer produces increasing strain, u_{sat} , must be at least -500 ppm. This is well comparable with that of PMN-PT15, for which $u_{sat}\approx1000$ ppm, and far above the saturation strain for 10 mol% Gd-doped ceria^{4, 14}, $u_{sat}=-12$ ppm. However, in contrast to classical electrostrictors, such as PMN-PT relaxor ferroelectrics, $Zr_{0.1}Ce_{0.9}O_2$ ceramics do not display any sign of ordering or of a "diffuse phase transition" $^{26-28}$ within the temperature range: -150 °C to +150 °C. But rather, the frequency-dependent, relative dielectric permittivity as a function of temperature (see Supporting information, Figure S1) simply increases with increasing temperature.

By probing local bonding patterns with extended X-ray absorption fine structure (EXAFS) measurements as well as with density functional theory (DFT) 24 simulations, we attributed the differences in behavior of aliovalent- and Zr-doped ceria to the large elastic dipole associated with the anharmonic motion of Zr in the latter system, especially when the Zr-concentration is low. This dipole is dynamic (*i.e.*, it is induced by the electric field), unlike aliovalent doped ceria, where elastic dipoles are preexisting, *i.e.*, they exist in the absence of an applied field²⁹. Dynamic elastic dipoles are associated with the presence of Zr^{+4} ions, for which the Shannon crystal radius is \sim 13% smaller than that of the host Ce^{+4} ions. In comparison to the corresponding volume of $[CeO_8]$ units in their Ce cage, the smaller $[ZrO_8]$ -local bonding units can roam in a larger space with a relatively low energy penalty. As a result, $[ZrO_8]$ -local bonding units are readily polarizable

producing a six-fold increase in the relative dielectric permittivity between undoped and Zr-doped ceria²⁴.

We have also reported that the electrostriction strain coefficient of $Zr_{0.1}Ce_{0.9}O_2$ ceramics increases exponentially with Zr content between 0-10mol% (see supplementary information in 24). The oxidized samples contain $\approx 100\pm10$ ppm of Ce^{3+} , while the partially reduced samples contain 1000-500 ppm of Ce^{3+} . For 10 mol% Zr, the oxidized samples displayed a longitudinal electrostriction strain coefficient ($M_{33} = u_{33}/E_3^2$) of $-10^{-16} \pm 10\%$ m²/V², which is the value expected by linear extrapolation of the dependence of M_{33} on Shannon crystal radius $^{14, 24}$. $|M_{33}|$ for the partially reduced samples was more than one order of magnitude smaller, which raises two central questions for the current study: (1) Can we provide evidence that non-classical electrostriction of Zr-doped ceria derives from a collective effect, *i.e.*, beyond the dilute approximation? (2) Can we identify the species which are responsible for depressing electrostrictive strain in reduced samples?

Finding answers to these questions is essential for understanding NCES in the presence of dynamic elastic dipoles and for future practical application of these materials under ambient conditions. To address these questions, we have investigated electrostrictive strain, as well as the mechanical and dielectric properties of 10 mol% Zr-doped ceria co-doped with 0.5 mol% of acceptor dopants (Sc, Yb, La or Ca). Combining experimental data with DFT-based simulations, we provide evidence that oxygen vacancies perturb the Zr-related dynamic elastic dipoles. Even a small concentration of oxygen vacancies is sufficient to produce a major change in the second coordination shell of Zr, and in the electromechanical response.

2 Materials and Methods

Methods used in this study paralleled those of Ref. 24 for which singly doped ceria ceramics - $Zr_xCe_{1-x}O_2$ (0 < x < 0.2) were prepared. The co-doped $Zr_{0.1}Do_{0.005}Ce_{0.895}O_{1.9975}$ (Do=Sc, Yb, La), $Zr_{0.1}Ca_{0.005}Ce_{0.895}O_{1.995}$, ceramics were prepared as described in ref. 24 . The motivation for the particular set of 0.5mol% acceptor co-dopants chosen was to cover a broad range of crystal radii, both larger and smaller than that of the host cation Ce^{4+} , as well as to sample valence other than 3+, while maintaining the vacancy concentration small but controlled (0.125 mol% for trivalent dopants). The crystal radii of trivalent dopants Sm or Gd , well known to provide large electrostrictive strain at frequencies \leq 1Hz, are similar to each other and somewhat larger than that of the host cation Ce.

Energy dispersive X-ray spectroscopy (EDS) of the ceramic surface was used to verify experimental stoichiometry (See Supporting Information, Table S1). Nominal stoichiometry is cited in the main text. The rapid sintering protocol, described previously 14,30 , was used to suppress possible cation segregation 31 . Samples with composition $La_{0.1}Ce_{0.9}O_{1.95}$ and $Yb_{0.1}Ce_{0.9}O_{1.95}$ were used as references for selected properties. The dimensions of all ceramic pellets were 10 mm diameter by 0.8-2 mm thickness. Porosity of the sintered pellets was determined from the mass density as measured by the Archimedes technique. All pellets were mirror polished with top and bottom faces made parallel. The pellets were heated at 773K for 5 h in pure oxygen to compensate for possible oxygen loss during sintering. Data for $Zr_xCe_{1-x}O_2$ (0 < x < 0.2) are from Ref. 24 and presented for comparison. These ceramics changed color from green-black, immediately following sintering, to yellow-white. When $x \le 0.1$, reoxidation resulted in a concentration of $Ce^{3+} \le 100$ ppm. However, when x = 0.2, the fraction of reduced Ce (i.e., Ce^{3+}) was $\ge 100 \text{ ppm}$ even after reoxidation. In the absence of reoxidation, the $Zr_{0.1}Ce_{0.9}O_2$ ceramic contained $\approx 500 \text{ ppm}$ Ce^{3+} .

Co-doped samples with 0.5 mol% of aliovalent dopants, *i.e.*, Zr_{0.1}Do_{0.005}Ce_{0.85}O_{1.9775} (Do=Sc, Yb, La) or Zr_{0.1}Ca_{0.005}Ce_{0.85}O_{1.998}, showed no change in color during re-oxidation, remaining yellow-white. The concentration of Ce³⁺ ions was determined from SQUID magnetometry as described in Ref. ²⁴.

Longitudinal (*i.e.*, parallel to the applied electric field) **electrostrictive strain**, u_{33} , was measured as described previously^{4, 32}. Briefly, the ceramic pellet was inserted between two stainless steel electrodes, with the top electrode being spring loaded. The displacement, δ , of the top-surface under voltage was measured with a proximity sensor (± 0.02 nm) monitored with a lock-in amplifier. Only alternating sine-wave voltage was applied to the sample and only second harmonic response was detected. The electrostriction coefficient in such configuration is given by: $M_{33} = \delta \cdot th / U^2$, where U is the voltage applied and th is the sample thickness measured with the accuracy ± 2 µm. The values of strain and electric field were calculated as $u = \delta/th$ and E = U/th. Measurements were performed under ambient conditions (297 \pm 2 K, relative humidity: 20% - 55%). Commercial samples of PMN-PT with silver contacts (TRS Technologies) and a 100-cut quartz single crystal without additional sputtered metal contacts were used for calibration of the measurement setup. Values matching literature data were obtained: M_{33} (PMN – PT) = (3.5 \pm 0.5) \cdot 10⁻¹⁶m²/V² and d_{33} (100 quartz) = 2.3 \pm 0.2 pm/V within the frequency range: 0.15 – 1000 Hz.

Impedance spectroscopy measurements to estimate relative material dielectric permittivity and total electrical conductivity were conducted at 298 K with a Novocontrol Alfa dielectric analyzer in the high voltage mode within the frequency range 1 mHz-1 MHz under excitation voltage of U_{AC} =10 V (electric field \approx 0.1 kV/cm for all samples). Constant bias was not applied (U_{DC} =0).

Measured impedance values fall within the 1% accuracy range of the impedance analyzer. Total conductivity, σ , and the relative material dielectric permittivity, ε , were estimated as:

(1)
$$\sigma = \frac{Z_{Re}}{|Z|^2} \frac{th}{A_c} \text{ and } \varepsilon = -\frac{Z_{Im}}{2\pi f \cdot \varepsilon_0 \cdot |Z|^2} \frac{th}{A_c},$$

where A_c is the area of the contacts, $Z = Z_{Re} + iZ_{Im}$ is the complex impedance, f is the frequency and ε_0 is the vacuum permittivity. Temperature dependent measurements were conducted in vacuum.

EXAFS (Extended X-ray absorption fine structure) spectra at the Zr K-edge and Ce L₃-edge were collected in fluorescence mode from 50 micron (300 mesh) powders (made by grinding pellets that had been used in electrostriction measurements) at the QAS (7-BM) beamline at the National Synchrotron Light Source-II (NSLS-II) at Brookhaven National laboratory. Data processing was carried out using the Athena and Artemis programs included in the Demeter data analysis package³³. For each element (Zr or Ce) absorption edge, multiple spectra (up to 30 scans) were averaged, to increase the signal-to-noise ratio. The X-ray absorption near edge structure (XANES) spectra at the Zr K-edge and Ce L₃-edge were pre-edge subtracted and edge-step normalized, and EXAFS data were obtained following established procedures. FEFF6 theoretical code was used for calculating photoelectron scattering amplitude and phase shifts. The data were fit using a non-linear, least square Levenberg-Marquardt algorithm in r-space, using Fourier transform of both data and model. For non-linear fitting of the theoretical EXAFS equations to experimental spectra, corrections to the model Zr-O and Zr-Ce distances (Δr), variance, *i.e.*, mean square relative displacements (σ^2) of r, and the correction to the photoelectron energy origin (ΔE) - the same for the Zr-O and Zr-Ce paths - were varied in the k-range and r-range intervals of 3-14 Å-1 and 1.5-3.9 Å, respectively. Third cumulants of the nearest neighboring pairs were also varied but those did not affect the fit quality. EXAFS spectra of Zr foil were fit as in Ref. 24 to obtain the amplitude reduction factor (0.99) which was then applied in fitting the spectra of the Zr-doped ceria (see supplementary material in Ref. ²⁴).

Theoretical modeling followed the procedures described in Ref. ²⁴. Plane-wave density functional theory (DFT) calculations were performed with the Vienna ab initio Simulation Package (VASP). The generalized gradient approximation (GGA) of Perdew, Burke, and Ernzerhof (PBE) 34 was used for the DFT exchange correlation functional with Hubbard-U correction (U_{eff} = 4.5 eV) for Ce 4f orbitals. ³⁵ The U value was selected according to Fabris et al.³⁶, which has been shown to provide satisfactory charge localization on Ce due to oxygen vacancy formation in the bulk and at the surface.³⁷ The projector-augmented-wave (PAW) method³⁸ was used, with valence electron configurations of Ce(5s²5p⁶6s²4f¹5d¹), Zr_sv $(4s^24p^65s^14d^3)$, and O $(2s^22p^4)$. The plane-wave cutoff energy was set to 500 eV with $2 \times 2 \times 2$ Gamma centered K-mesh for the $2 \times 2 \times 2$ simulation cell with 96 atoms. The DFT relaxed lattice parameter is 5.495 Å agreeing well with experiments¹⁴. The electronic and atomic relaxation convergence criteria were 1×10^{-6} eV and 0.01 eV Å⁻¹, respectively. To avoid a false symmetric vacancy state seen in some DFT calculations, ³⁹ atoms near the vacancy and the dopants are initially shifted by 0.1 Å. Symmetry is not imposed during structural relaxation. For ab initio molecular dynamics (AIMD) calculations, NVT ensemble (temperature 300K; volume maintained unchanged from the DFT minimized value in order to isolate the dynamic effect) was used. Structural characteristics were averaged for 4ps with a timestep of 1 fs.

AIMD-EXAFS simulations were performed as follows. The last 2ps of the AIMD trajectories were segmented into frames and expanded around a central Zr absorber using the OVITO API ⁴⁰. For each frame, FEFF10⁴¹was used to calculate K-edge EXAFS for the central Zr absorber. For

simulations with 2 Zr, two frames were generated, each with a central Zr, and EXAFS was calculated per frame. FEFF10 was run with S02=1, EXAFS=20, RPATH=7, NLEG=8, CRITERIA=0.00 1.5, EXCHANGE= 0 0 0. The resulting EXAFS spectra were analyzed and averaged with Larch⁴² and Athena⁴³. All calculations were performed on the Brookhaven National Laboratory Center for Functional Nanomaterials Institutional Cluster.

3 Results and Discussion

3.1 Structure, lattice parameter

According to X-ray diffraction (XRD) patterns, all ceramics $Zr_{0.1}Do_{0.005}Ce_{0.895}O_{1.9975}$ (Do=Sc, Yb, La), $Zr_{0.1}Ca_{0.005}Ce_{0.895}O_{1.995}$, $La_{0.1}Ce_{0.9}O_{1.95}$ and Yb_{0.1}Ce_{0.9}O_{1.95}, are single-phase fluorite (space group 225, Fm $\overline{3}$ m) ceramics with random crystallite orientation. Samples with composition $La_{0.1}Ce_{0.9}O_{1.95}$ and Yb_{0.1}Ce_{0.9}O_{1.95} were used as reference for selected properties. The mean grain size, as estimated by the lineal intercept method⁴⁴ from SEM images of the pellet circumferential surfaces, decreases with Zr addition from 3 μ m at 5 mol% to 1 μ m at 10 mol%. Co-doping with 0.5mol% Sc, Yb, La or Ca does not detectably change the grain size. All samples were <3% porous, which allowed accurate correction ^{45,46} of the Young's (*Y*) and shear (*G*) moduli calculated from ultra-sound time of flight measurements (see SI in ref. ²⁴). As reported earlier ²⁴, the lattice parameter (Figure 1) decreases with increase in Zr content due to the much smaller crystal radius of Zr⁴⁺ with respect to Ce⁴⁺. Co-doping of Zr_{0.1}Ce_{0.9}O₂ with 0.5mol% of aliovalent dopants does not significantly affect the unit cell size, as expected. (Figure 1b).

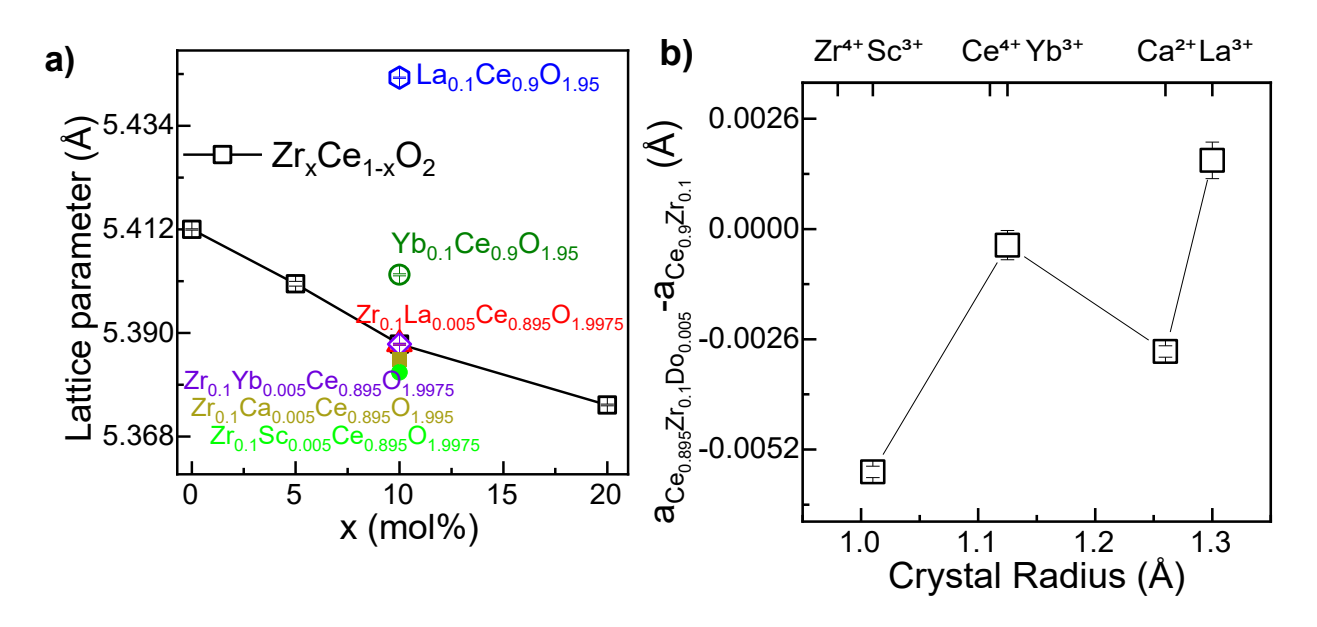


Figure 1. (a) Lattice parameters of oxidized ceramics prepared for this study calculated by linear regression based on the indexing of 10 diffraction peaks according to $Fm\overline{3}m$ symmetry. The data for $Zr_xCe_{1-x}O_2$ are from ref. ²⁴, the data for $La_{0.1}Ce_{0.9}O_{1.95}$ and $Yb_{0.1}Ce_{0.9}O_{1.95}$ are given for comparison. **(b)** Change in the lattice parameter of the co-doped 10ZDC ceramics as a function of the crystal radius of the aliovalent co-dopant.

3.2 Electrostriction measurements

For all ceramic samples, as also noted previously²⁴ for fully oxidized 10ZDC, strain vs the square of the applied electric field remains linear for $E \le 17 \text{kV/cm}$ (the highest field used in this study), indicating that for all samples: (1) this value is far below saturation field; and (2) any changes in dielectric permittivity due to increasing electric field must be very small. See also Fig S1D. Codoping $Zr_{0.1}Ce_{0.9}O_2$ with 0.5 mol% of acceptor dopants (Zr:Do = 20:1) introduces 1250 ppm (for Ca 2500 ppm) of vacancies into the oxygen sub-lattice. However, this is sufficient to reduce the longitudinal electrostriction strain coefficient by an order of magnitude with respect to oxidized $Zr_{0.1}Ce_{0.9}O_2$ (Figure 2). This change is displayed by all co-dopants within the frequency range 0.1 Hz-100 Hz despite the significant difference in crystal radius. From these measurements, we conclude that the factor suppressing the electrostriction effect must be the presence of oxygen vacancies.

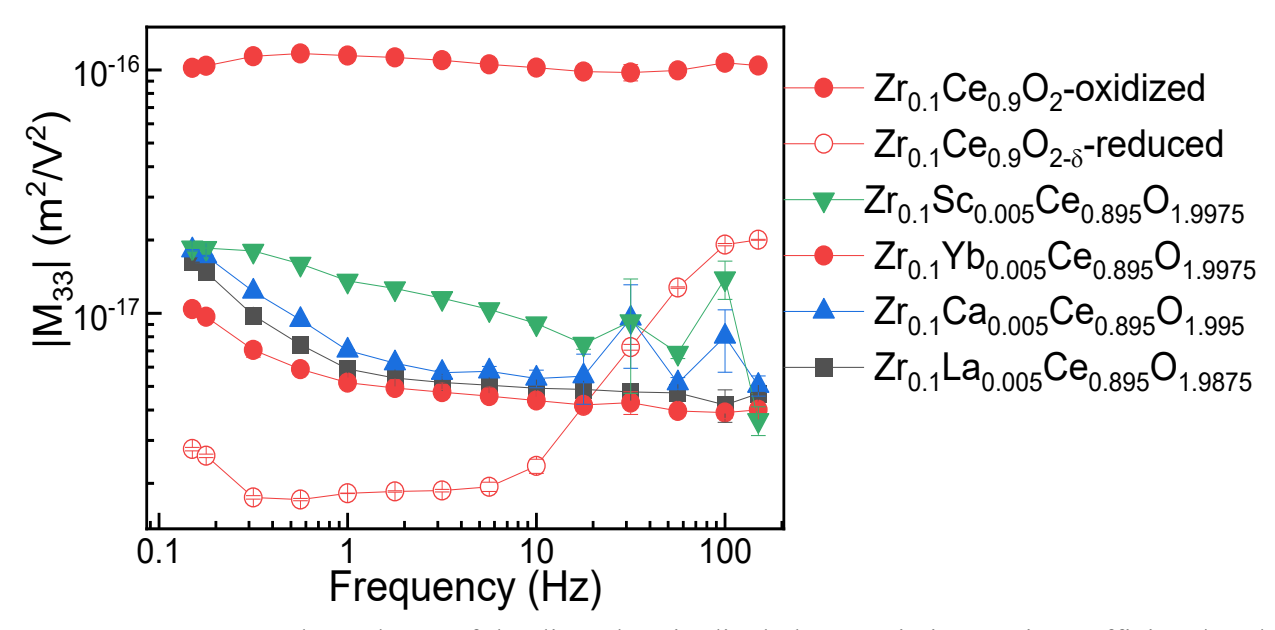


Figure 2. Frequency dependence of the direct longitudinal electrostriction strain coefficient $|M_{33}|$ of 10ZDC ceramics with and without aliovalent co-doping. Measurements were made in triplicate under ambient conditions; in some cases, error bars are smaller than the symbols. Note that the data on the reduced 10ZDC is not fully reproducible as the concentration of vacancies is hard to control unless the sample is oxidized. The concentration of Ce^{3+} in the oxidized 10ZDC was <100 ppm²⁴.

The inverted frequency response of the reduced 10ZrDC ceramics is difficult to explain: Ce³⁺ ions and the corresponding concentration of oxygen vacancies for charge compensation are both present. They certainly must modulate the electrostrictive response; and while the perturbing effect of the presence of oxygen vacancies is demonstrated in the current work, the effect of Ce³⁺ ions remains unknown. The concentration of Ce³⁺ is difficult to control in 10ZrDC under ambient conditions. On the other hand, the concentration of oxygen vacancies is controllable *via* aliovant doping. Therefore, investigating the effect of the Ce³⁺ ions on 10ZrDC electromechanical properties must lie outside the scope of this report.

3.3 Elastic modulus

As reported in ref. 24 , introduction of isovalent Zr lowers the elastic modulus of ceria as measured with USTOF (Figure 3) from 227±1 GPa (pure ceria) to 213 ± 0.1 GPa (10 mol% Zr), i.e., 62±4% per mol of the dopant even though Zr-doping does not reduce the number of chemical bonds in the

lattice. This change is more striking than doping with Gd (48 mol% ³²), even though Gd³⁺ does lower the number of chemical bonds due to oxygen vacancy formation. Based on EXAFS analysis results and DFT modeling, this effect was attributed to the fact that an off-center displacement of Zr with respect to its coordination shell is energetically far less costly than that for the Ce-host²⁴, allowing [ZrO₈] local bonding units some freedom to shift with respect to the next nearest coordination shell. The introduction of 0.5 mol% co-dopant increases the elastic modulus. For Yb³⁺, the increase is within the margin of error; however, for the other co-dopants, the increase is well beyond the uncertainty. For La³⁺ co-doping, the elastic modulus increases to 219±2.8 GPa, which corresponds to 563±263% per mol of co-dopant (Figure 3), which is much larger than that produced by Zr or Gd in ceria. For Sc³⁺ and Ca²⁺ co-doping, the effect is even more pronounced (Figure 3b), indicating that the aliovalent dopant produces major changes in the chemical bond stiffness without a significant change in the lattice parameter.

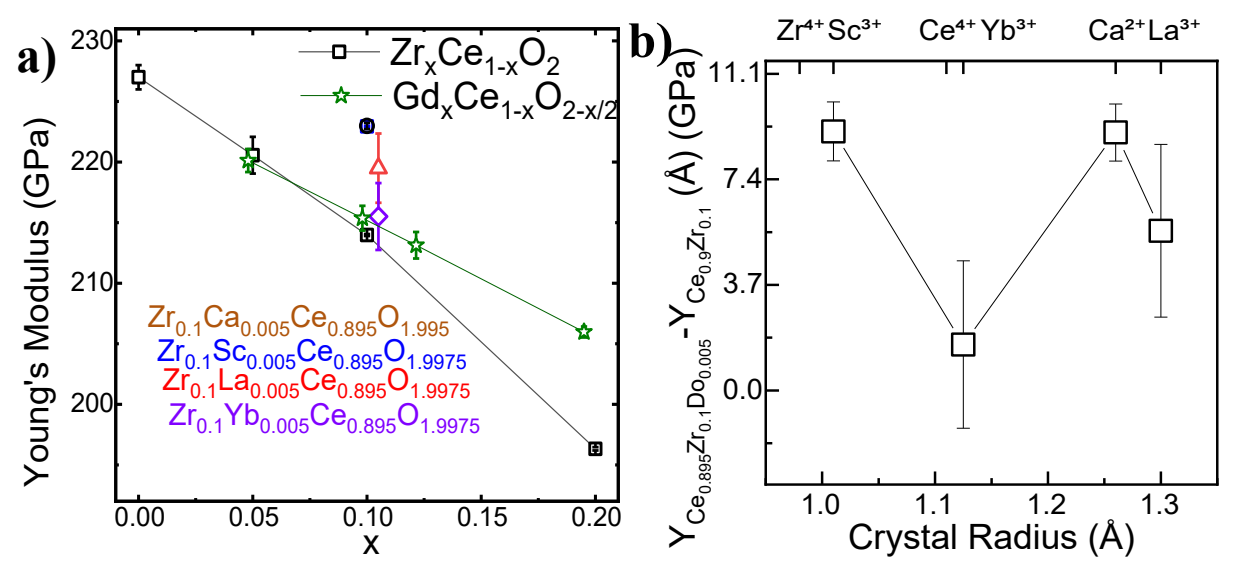


Figure 3. (a) Young's modulus of aliovalent co-doped 10ZDC ceramics. The data for $Zr_xCe_{1-x}O_2$ from ref. ²⁴ and $Gd_xCe_{1-x}O_{2-x/2}$ from ref. ³² are shown for comparison. (b) Change in the Young's modulus of 10ZDC ceramics upon co-doping with aliovalent dopants as a function of the crystal radius of the co-dopant. Measurements were made with USTOF as described in the Materials and Methods section.

3.4 Dielectric permittivity

Nyquist plots of the impedance spectra for all ceramic samples under ambient conditions, as well as for 10ZDC as a function of temperature in vacuo, did not display complete semi-circular arcs (similar to ref. ²⁴); consequently, the real and the imaginary parts of the dielectric permittivity could only be approximated. (Figure S1) As we reported earlier ²⁴, doping ceria with Zr increases both the relative dielectric permittivity (ε_r , real component) and the total electrical conductivity. At a frequency of 100 Hz, relative ε_r of undoped oxidized ceria is $\varepsilon_{CeO_2}^{100Hz} \approx 32\pm5$, which is also close to the dielectric permittivity of pure ZrO_2 . However, doping ceria with Zr, produces a marked increase in the real and imaginary parts of the relative dielectric permittivity: $\varepsilon_{Zr_{0.05}Ce_{0.95}O_2}^{100Hz} = 62\pm1$ and $\varepsilon_{Zr_{0.1}Ce_{0.9}O_2}^{100Hz} = 224\pm2$ for oxidized samples with ≤ 100 ppm Ce^{3+} (Figure 4a). The total conductivity of oxidized samples at 100 Hz (Figure 4c) increases even more dramatically, up to two orders of magnitude for $\text{Zr}_{0.1}Ce_{0.9}O_2$, with respect to CeO_2^{-24} .

Co-doping Zr_{0.1}Ce_{0.9}O₂ with 0.5 mol% of aliovalent dopants restores the relative dielectric permittivity to values comparable to undoped ceria or to Yb_{0.1}Ce_{0.9}O_{1.95} (Figure 4a; Figure 4b as a function of co-dopant crystal radius), while the effect on the total electrical conductivity is not monotonic: for La and Yb, total conductivity decreases, while for Sc and Ca, it remains almost unchanged (Figure 4c; Figure 4d as a function of co-dopant crystal radius).

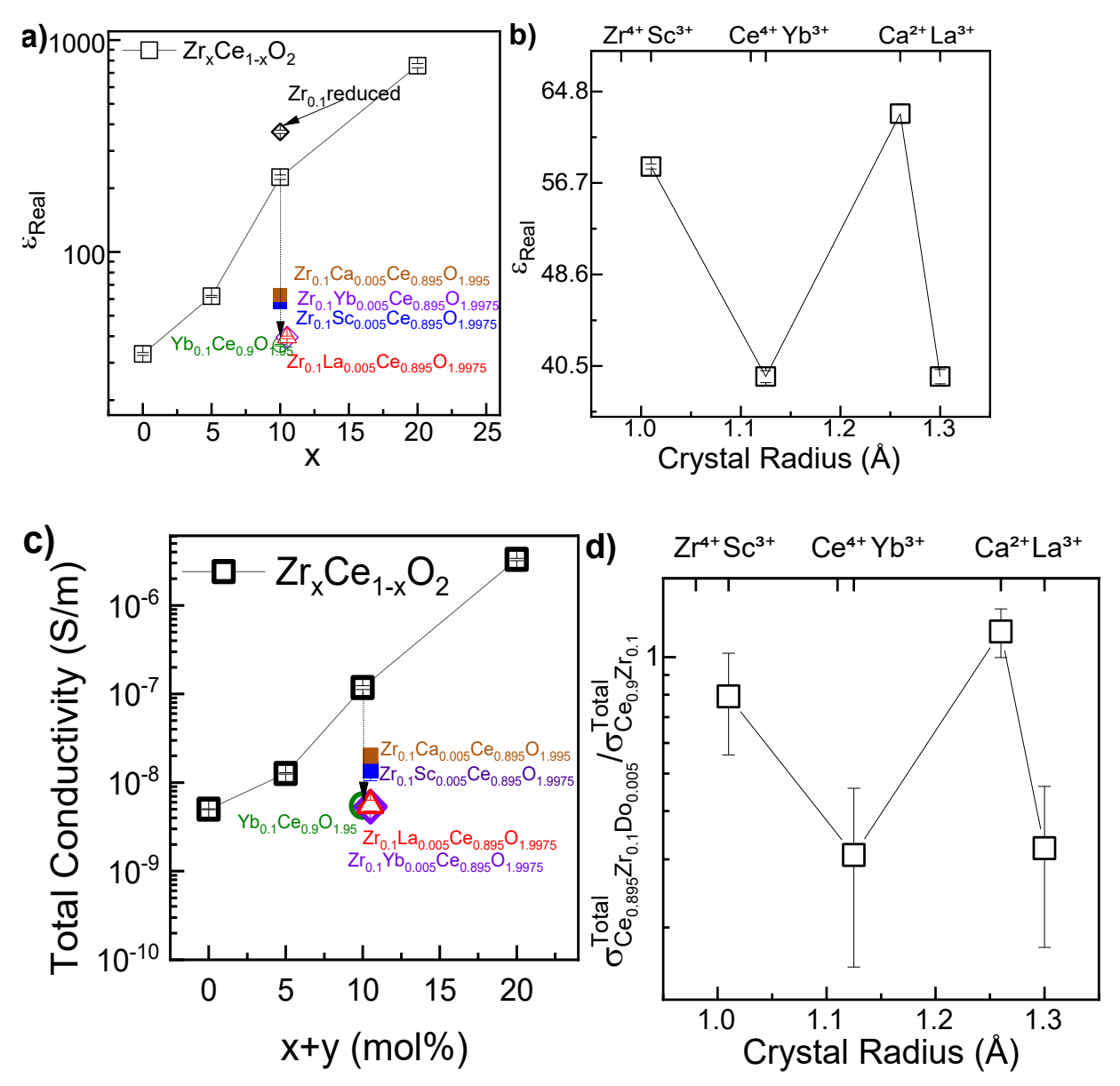


Figure 4. (a) Real component of the complex relative dielectric permittivity of sintered and re-oxidized ceria $Zr_{0.1}Do_{0.005}Ce_{0.85}O_{1.9975}$ (Do=Sc, Yb, La) and $Zr_{0.1}Ca_{0.005}Ce_{0.85}O_{1.995}$ ceramics. The data are shown for $V_{ac} = 10$ volts, f = 100 Hz, with spring loaded electrodes. Two pellets with the same chemistry were each measured in triplicate. (b) The real component of the complex relative dielectric permittivity of the co-doped 10ZDC ceramics as a function of the crystal radius of the co-dopant. (c) Total conductivity at 100 Hz of the ceramics shown in (a). The data for $Zr_xCe_{1-x}O_2$ from ref. ²⁴ and $Zr_0Ce_{1-x}O_{2-x/2}$ from ref. ³² are shown for comparison. Conductivity of reduced $Zr_0Ce_{0.9}O_2$ is not shown as it is not reproducible due to variability of oxygen content in reduced samples. (d) Total conductivity of 10ZDC ceramics upon co-doping with aliovalent dopants, normalized to the total conductivity of 10ZDC, as a function of the crystal radius of the co-dopant.

3.5 Changes in the local structure (EXAFS)

Introduction of 0.5 mol% Sc, Yb, La or Ca into Zr_{0.1}Ce_{0.9}O₂ ceramics produces significant changes in the longitudinal electrostriction coefficient and mechanical and dielectric properties (Sections 3.1-3.4 above), suggesting a major change in local structure. Since all co-dopants produce similar effects, despite large differences in crystal radii (101 pm for Sc vs 130 pm for La) and are introduced in a very small amount, the changes are most likely expected in Zr-bonding patterns. We have therefore investigated perturbation of the Zr K edge EXAFS spectra of powdered ceramics in the presence of Yb³⁺ co-doped into 10ZDC. EXAFS analysis results obtained for the Zr edge in the oxidized and Yb-co-doped sample powders, are summarized in Table 1. 0.5mol% Yb co-doping, with resulting 1250 ppm of oxygen vacancies, shortened the average Zr-O (1st nearest neighbor) and Zr-Ce (2nd nearest neighbor) shell distances compared to those in the undoped sample. Visual examination of the raw data (Figure 5a,b) and the fact that the mean square relative disorder describing Zr-Ce bonding increases upon Yb-doping (Table 1) shows that the dominant effect of Yb co-doping is the introduction of strong disorder into the second coordination shell. We have further examined the effect of Yb co-doping on Ce L₃ edge EXAFS data (Figure 5c) and found that the first (Ce-O) and second (Ce-Ce/Zr) shell of Yb codoped samples have lower intensity compared to the 10ZDC samples. Similar to the spectra obtained at the Zr K-edge, those obtained at the Ce L₃-edge also testify that the presence of 1250 ppm of V_0 affect most Zr ions as well as the Ce-host by introducing a disordering effect in the lattice.

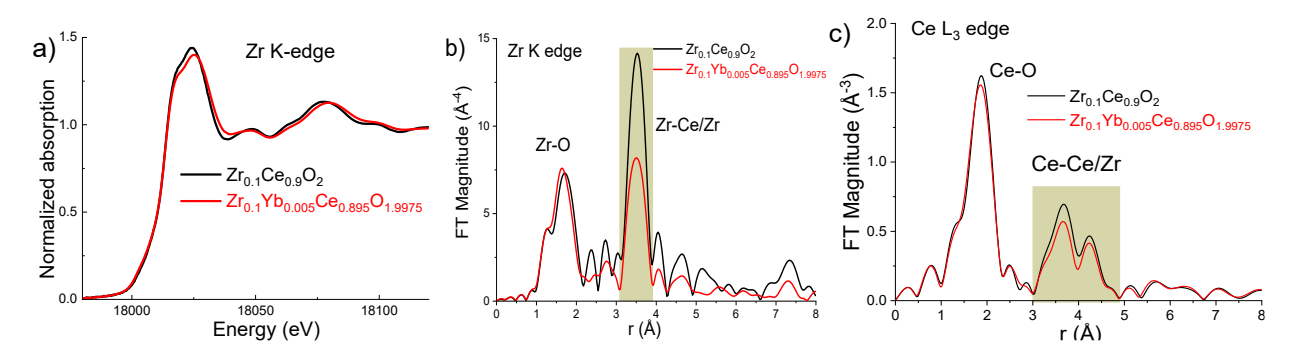


Figure 5. (a) Zr K-edge XANES data and (b) EXAFS data in r-space for 10ZDC powder samples with and without Yb co-doping. The k-range for Fourier transforms was from 3 to 14 Å⁻¹ and k³ weighting was used. The relatively lower intensity of the second shell **(b)** contribution to EXAFS indicates enhanced disorder in the second (Zr-Ce) coordination shell for the Yb-doped sample. **(c)** Fourier transform magnitudes of the k²-weighted Ce L₃-edge EXAFS data of the pure and Yb-co-doped 10ZDC. The k-range from 2 to 9 Å⁻¹ was used for Fourier transforms. The Yb-co-doped EXAFS displays lower intensity in the first (Ce-O) and second (Ce-Ce/Zr) shells as compared to the 10ZDC powder sample, indicating that co-doping with 0.5mol% Yb introduces a disordering effect into the local environment.

Table 1 Results of EXAFS analysis for Zr-O and Zr-Ce first and second nearest neighbor distances and their mean squared displacements.

Sample	R_{Zr-O} (Å)	$\sigma^2_{Zr-O}(\mathring{A}^2)$	R _{Zr-Ce} (Å)	σ^2 Zr-Ce (Å ²)
10ZDC with Yb	2.18(1)	0.0092(13)	3.76(1)	0.0086(5)
10ZDC (Oxidized)	2.23(1)	0.0091(14)	3.79(1)	0.0062(3)

3.6 DFT modelling of local bonding and dynamics of $[ZrO_x]$ -and [Zr-Zr-Oy]

The probability that in doped ceria with mol fraction of dopant cation x, there are n-dopants in the second coordination shell (CN=12) is given by the binomial distribution:

(2)
$$P(x,n) = \frac{\text{CN!}}{n!(\text{CN}-n)!} \cdot x^n \cdot (1-x)^{\text{CN}-n}.$$

The probability of finding at least one Zr atom out of the CN=12 cations in the second coordination shell in 10ZDC is $1 - P(0.1, 0) \approx 0.718$, predicting that most Zr ions will have at least one Zr neighbor. It is therefore important to examine the case with a Zr-O-Zr structure, *i.e.*, the non-dilute

case. We first illustrate the difference between single-Zr and Zr-pair doped CeO₂. For single Zr^{4+} doping, one Zr ion was introduced by replacing one of the Ce ions. The supercell contains $Zr_1Ce_{31}O_{64}$, with all Ce 4+. This single-Zr doped CeO₂ simulation can be found in our previous work²⁴. In order to investigate the effect of more concentrated Zr doping *via* DFT modelling in the present study, two Zr atoms were introduced into the 96-atom 2 × 2 × 2 supercell, resulting in a $Zr_2Ce_{30}O_{64}$ system with all Ce cations 4+. All 31 combinations have been tested, and their energies are compared as shown in Table S2. The 2 Zr atoms occupying the 1NN cation positions are the most energetically favorable, although the energy difference is ≈ 0.1 eV. It is reasonable to expect that the ceramic preparation procedure will produce a random distribution of dopants, especially considering that the materials were subject to high temperature using a rapid sintering protocol³⁰. The 1NN Zr-pairs share two oxygen atoms, so we may characterize a [Zr-ZrO₁₄] unit in analogy to the [ZrO₈] cube.

The averaged radial distribution function analysis was performed for the last 2ps 300K AIMD trajectories as shown in **Figure 6**c,d (solid blue lines), where 1Zr doped CeO₂ system was included as a dilute case comparison. A more quantitative analysis was provided in the same figure through bond length variation calculations as in ref. ²⁴, where the reduced average Zr-O bond length and increased Zr-Ce variations are clearly captured. As claimed in ref. ²⁴, Zr-O bond variations are 3 to 4 times larger in AIMD results than experimentally measured (Table 1), possibly due to the strong anharmonicity of the Zr-O bond, captured in the simulations, but which is known to cause underestimation of the bonding variation by conventional EXAFS analysis methods. The computed bonding variation value of 0.044 Å² is approximately twice as large for the non-dilute 2 Zr case, as compared to 0.024 Å² for the dilute 1 Zr case. We further probed the energy cost for the correlated motions of Zr-pairs, indicated here as "in phase" and "out of phase" (as shown in

Figure S2), where "in phase" means simultaneous displacements of two Zr atoms along a given crystallographic direction, while "out of phase" means simultaneous inward or outward displacements of two Zr atoms. We found that the stiffness of two neighboring -[ZrO₈] units is the lowest when displacement is in phase and along the direction that points from one Zr to the other (*i.e.*, one Zr ion promotes in-phase displacement of the neighboring ions, so that collective motion is favored). Out of phase and other crystallographic directions of in-phase displacement are more costly in energy, where such strong anisotropic behavior of two Zr atoms indicates a possible collective displacement mode. Considering the much larger Zr-O anharmonicity (than Ce-O anharmonicity) and possible collective Zr-Zr displacement, the electrostrictive strain exhibited an exponential increase with Zr doping concentration from dilute to non-dilute (10mol%), instead of showing a a simple linear relation with Zr-doping concentration (see Figure 3 in ref. ²⁴).

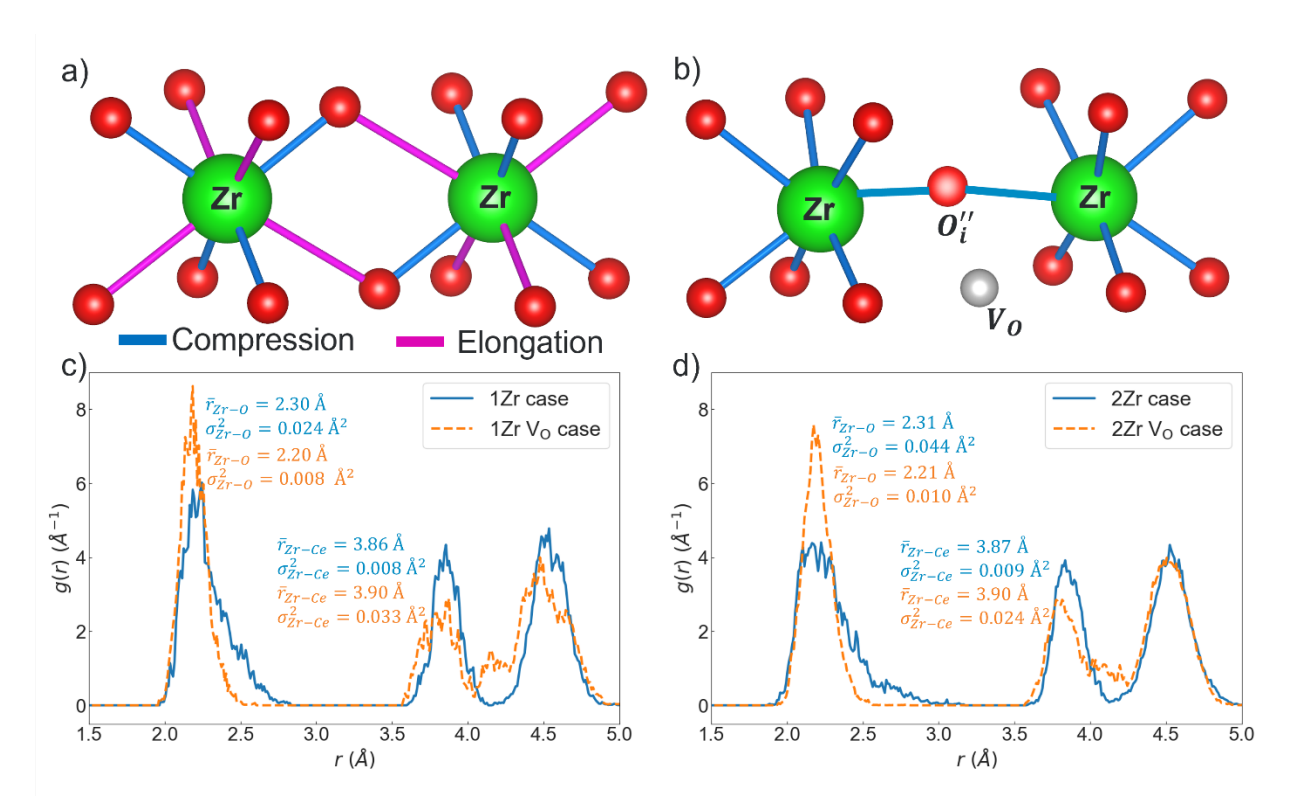


Figure 6. a). Two neighboring Zr and the local bond distortions are shown. Blue color indicates bond compression while pink color indicates bond elongation (compared to Zr-O length 2.27 Å in 1 Zr doped CeO_2 dilute case). b). When V_O (silver color) is introduced into the local bonding

system, an oxygen atom which is shared by 2Zr (highlighted in light red) undergoes a hopping motion to a location between 2 Zr atoms, creating an additional V_0 and an interstitial oxygen O_i'' . The Zr-centered radial distribution function (RDF) for the bulk case (blue) and the vacancy-containing case (orange) was applied to the last 2ps 300K AIMD trajectories for a 1 Zr (c) and 2 neighboring Zr (d) containing supercell.

3.7 Modelling the effect of vacancies on $[ZrO_x]$ and [Zr-Zr-Oy] local bonding units

Measurements have shown that the introduction of an oxygen vacancy will lower the magnitude of the electrostriction strain coefficient, (see Figure 2), independent of whether the oxygen vacancy is due to sample reduction or to divalent/trivalent doping. Aliovalent doping allows more precise experimental control of the vacancy concentration. We chose to study the impact of oxygen vacancy (V_0) on the dynamics of Zr primarily based on the reduced system. Similar analyses were conducted for non-reduced V_0 with similar results and reported in Figure S5. As is generally true for dopants smaller than cerium in the fluorite lattice, a Zr-dopant traps oxygen vacancies very efficiently⁴⁷⁻⁴⁹. Even a few mol% of Zr in 10mol% Sm-doped ceria lowers ionic conductivity by up to five orders of magnitude⁴⁸. We therefore suggest that it is possible that all V_0 introduced by the aliovalent co-dopants or by reduction may be trapped by Zr_{Ce} .

In 3% (1 out of 32) of anion sites in Zr-doped ceria, one oxygen atom was removed to create an oxygen vacancy (V_O). Magnetic moment calculation confirmed that the structure is $Zr^{4+}Ce^{3+}{}_2Ce^{4+}{}_{29}O^{2-}{}_{63}$ following relaxation. We first compare the site selection and cation oxidation state change due to the presence of an V_O . The V_O formation energy ($E_{V_O}^f$) may be calculated according to $E_{V_O}^f = E_{V_O} - E_{bulk} + \mu_O^{FERE}$, where μ_O^{FERE} is the fitted elemental reference energy 50 , for V_O sited at different distances from the Zr cation, *i.e.*, from 1NN to the fourth nearest neighbor (4NN). The resulting $E_{V_O}^f$ are listed in Table 2. During V_O formation, Zr remains 4+, while two of the Ce cations closest to the oxygen vacancy undergo 4+ to 3+ reduction. This process is similar

to the generation of intrinsic oxygen vacancies in bulk CeO₂, *i.e.* far from the dopant Zr^{4+} , and requiring a formation energy of ~3.1 eV. Approximately 0.60 eV less energy is required to generate $E_{V_0}^f$ near the Zr^{4+} dopant, clearly reflecting the V_0 trapping effect of the smaller radius Zr cation.

Table 2 Oxygen vacancy formation energy in 3% (1 out of 32) Zr doped ceria 96-atom supercell. The distance of the O vacancy to the Zr atom is also listed.

Distance to Zr in bulk structure (Å)	Vacancy formation energy (eV)	
2.282	2.50	
4.545	3.29	
5.985	3.18	
7.144	3.11	
"Far from " Zr in the CeO ₂ bulk	3.12	

When modelling a single oxygen vacancy (V_0) introduced into a Zr-pair (2 Zr) doped CeO₂ supercell, the Vo site is chosen by removing one of the two oxygen atoms shared by two Zr cations (**Figure 6b**). Magnetic moment calculation confirmed that the structure is $Zr^{4+}_2Ce^{3+}_2Ce^{4+}_{28}O^{2-}_{63}$ following relaxation. The resulting formation energy drops from 2.50 eV in the 1 Zr case to 1.85 eV, revealing a much deeper trapping effect. Dramatic local structure reorganization is also observed. The remaining oxygen, shared by the Zr-pair, undergoes hopping to a site between the Zr atoms, becoming a new interstitial oxygen $O_i^{\prime\prime}$ and leaving an additional V_0 on the lattice (**Figure 6b**). This movement results in two Zr- $O_i^{\prime\prime}$ bonds that are similar in length to Zr-O bonds in ZrO₂, as well as a narrowing of the Zr-O bond length distribution as shown in Figure S3, Figure S4 and **Table S3**. The DFT calculated structure provides a theoretical basis for a disturbed second shell: creation of $O_i^{\prime\prime}$ that repels both Zr ions, leading to an increase in Zr-Zr distance from 3.96 Å to 4.21 Å and a broader Zr-cation distribution as observed by EXAFS. The presence of V_0 also

pins the dynamic elastic dipole and the correlated motions of Zr-pairs. **Figure 6**c,d demonstrate that with the introduction of V_0 , two obvious changes can be detected in the shape of the radial distribution function (RDF): 1) the formerly anharmonic Zr-O peak within the range 2.0~3.0 Å becomes sharp and harmonic; 2) a less intense Zr-cation peak with additional, even weaker, peaks appearing within the range 3.5~4.5 Å. The off-equilibrium energy landscape in Figure S2 shows a systematically increased energy cost when comparing vacancy-containing off-center motion with their zero-vacancy counterparts. The lability of both $[ZrO_x]$ and $[Zr - Zr - O_y]$, which is the primary driving force for dynamic elastic dipoles in Zr doped ceria, is eliminated. This may provide an explanation for the reduction in electrostrictive strain upon 0.5mol% La or Yb codoping. The model should also explain the decrease in dielectric constant: stiffer bonding in the $[ZrO_7]$ units is expected to markedly decrease polarizability.

We note that introducing an oxygen vacancy into Zr doped ceria is not identical to the appearance of charge compensating Vo due to the presence of a trivalent dopant. In the former case, Ce experiences a 4+ to 3+ reduction, while in the latter case, the trivalent dopant is, of course, in a 3+ oxidation state, and all Ce atoms are 4+. To verify that the reduced Zr doped ceria can correctly reflect the structure and dynamic properties of a small amount of trivalent dopant in 10mol % Zr doped ceria, 2 electrons were removed from the Zr₂Ce₃₀O₆₃ structure. After relaxation, magnetic moment calculation confirmed a Zr⁴⁺₂Ce⁴⁺₃₀O²⁻₆₃ supercell. In these non-neutral supercells, the effect of a neutralizing background has been considered. Figure S5 shows similar RDF as the Zr₂Ce₃₀O₆₃ structure, indicating weaker Zr-Zr correlated motions.

The above conclusion matches a numerical estimate of the interaction distance between oxygen vacancies in trivalent co-doped 10ZDC (e.g. $Yb_{0.005}Zr_{0.1}Ce_{0.895}O_{1.9975}$). Anions form a simple cubic sub-lattice in the fluorite lattice with interanion distance, $\frac{1}{2}$ of the lattice constant, a. This

gives for the average distance between oxygen vacancies $d=1/\sqrt[3]{P_V} \cdot \frac{1}{2} \cdot a = 9.3 \cdot \frac{1}{2} \cdot a$, where $P_V=0.5\%/4=0.125\%$ is the fraction of V_0 on the oxygen sublattice. Each $[ZrO_7-V_0]$ unit can therefore perturb $[ZrO_8]$ -local bonding units at an interaction distance of at least $l_{int}=d/2=2.32$ unit cells =1.4nm. The number of cations surrounding a given anion site at a distance of 2.32 unit cells in the FCC cation sublattice is 200. Since the cations are expected to be randomly distributed, as noted previously, each $[ZrO_7-V_0]$ local bonding unit can potentially affect at least 200 $[cation-O_8]$ -local bonding units or at least 20 $[ZrO_8]$ -local bonding units in $Yb_{0.005}Zr_{0.1}Ce_{0.895}O_{1.9975}$.

3.8 Reconciling EXAFS spectra and ab initio molecular dynamics modelling by MD-EXAFS simulations.

It is possible to link our AIMD simulations directly to the EXAFS spectra by calculating theoretical EXAFS on the trajectories produced by AIMD using the approach known as MD-EXAFS^{51, 52}. Due to the short characteristic time of photoelectron scattering (much shorter than the time of a bond vibration), EXAFS can be considered as an average of static structural snapshots, equivalent to AIMD trajectories. This approach is a powerful method for directly validating or benchmarking MD simulations obtained with empirical force fields 53 , *ab initio* calculations 54 , and machine-learned force fields 55 . Here, we employ AIMD-EXAFS to see whether or not the perturbing effect of an oxygen vacancy (V_0) seen in AIMD simulations is also revealed in the EXAFS data.

Experimental EXAFS and AIMD-EXAFS are compared in Figure S6, where we look at the EXAFS spectra collected from oxidized $Zr_{0.1}Ce_{0.9}O_2$ and $Zr_{0.1}Yb_{0.005}Ce_{0.9}O_{1.9975}$ powder samples and the AIMD-EXAFS calculated for the 2Zr and 2Zr + V_0 case. Two key areas of interest are the first shell between ~1 and 2 Å (Zr-O bonds) and the second shell between ~3 and 4 Å (Zr-Ce bonds). We cannot compare the EXAFS to the AIMD-EXAFS quantitatively due to the DFT

functional's overestimation of the lattice constant, but we can still make a qualitative comparison. In the first shell, the trends are replicated: the intensity of $Zr_{0.1}Yb_{0.005}Ce_{0.9}O_{1.9975}$ is larger than $Zr_{0.1}Ce_{0.9}O_2$, and the intensity of $2Zr + V_0$ is larger than 2Zr; however, the magnitude of the difference is much larger in the AIMD-EXAFS. In the second shell, the trends are also replicated: the intensity of $Zr_{0.1}Yb_{0.005}Ce_{0.9}O_{1.9975}$ is smaller than $Zr_{0.1}Ce_{0.9}O_2$, and the intensity of $2Zr + V_0$ is smaller than 2Zr; here, the magnitude of the difference of the AIMD-EXAFS is in much better agreement with experiment.

The trend in the first shell was initially expected to be much larger in the AIMD-EXAFS because every Zr ion environment in our simulation box contains a vacancy, *i.e.*, the effect of the vacancy should be magnified in the AIMD-EXAFS. In the real sample, not every Zr has a vacancy neighbor; thus, experimental EXAFS can be understood as corresponding to a linear combination of Zr environments with and without vacancy, hence, a contrast between the theory and experiment was expected in the second shell. The magnitude of the changes in the second shell peak intensity of the MD-EXAFS is, however, almost the same as in the experimental data. This implies that Zr ions with and without vacancies in the experimental sample feel the same disordering effect in the second shell corresponding to the Zr-Ce/Zr interactions. Therefore, through AIMD-EXAFS analysis, we conclude that the collective effect due to the vacancy observed in the AIMD trajectories is able to explain trends observed in the experimental EXAFS data.

4 Conclusions

Combining XAS with DFT and AIMD modeling, and aided by MD-EXAFS simulations, this work provides evidence that non-classical electrostriction in Zr-doped ceria results from correlated displacement of dynamic elastic dipoles associated with $[ZrO_8]$ -local bonding units. Co-doping with 0.5mol% trivalent or divalent dopants (Sc, Yb, La or Ca) produces >10-fold reduction in the

longitudinal electrostriction strain coefficient; >3-fold reduction in the relative material dielectric permittivity; and a detectable increase in elastic modulus. Since these changes depend on neither the crystal radius nor valence of the co-dopant, we conclude that the responsible species are the oxygen vacancies introduced for charge compensation. For the trivalent co-dopants $(Do_{0.005}Zr_{0.1}Ce_{0.895}O_{1.9975})$, vacancies are present at a concentration ratio 1:40 with respect to Zr, giving a characteristic interaction distance ≈ 2.3 -unit cells=1.2 nm. Oxygen vacancies participate in $[ZrO_7 - V_0]$ local bonding units, disrupting the correlated motion of $[ZrO_8]$ -local bonding units. We suggest that the exponential increase in the longitudinal electrostriction strain coefficient with Zr-content for x<0.2 may also be explained in this way and should be taken into account for further development of non-classical electrostrictors based on Zr-doped ceria.

Acknowledgements

X-ray absorption spectroscopy studies and data analysis by A.I.F were supported by NSF Grant number DMR-2312690. I.L. acknowledges the BSF program grant 2022786 for his contribution to the XAS studies. These grants are the two parts of the NSF-BSF grant awarded to A.I.F. and I.L., respectively.

The work on development of the theoretical description and the properties of the elastic dipoles was supported by the Israel-US Binational Science foundation regular program (Y.Q. and I.L grant 2020108). The work on development of novel electrostrictive materials was supported by the US Army Research Office (ARO grant #W911NF2110263, I.L.).

This research used beamline 7-BM (QAS) of the National Synchrotron Light Source II (NSLS-II), a U.S. DOE Office of Science User Facility operated for the DOE Office of Science by Brookhaven National Laboratory under contract no. DE-SC0012704.. We acknowledge support of the beamline experiments by the Synchrotron Catalysis Consortium funded by the US

Department of Energy, Office of Science, Office of Basic Energy Sciences, Grant No. DE-SC0012335. This research used the Theory and Computation facility of the Center for Functional Nanomaterials (CFN), which is a U.S. Department of Energy Office of Science User Facility, at Brookhaven National Laboratory under Contract No. DE-SC0012704. We gratefully acknowledge Drs. Lu Ma and Steven Ehrlich for their support of the XAS measurements at the 7-BM beamline.

Supporting Information description

Supporting Information: Impedance spectroscopy and Bode - type plots for 10mol% Zr doped ceria as a function of AC frequency within the temperature range -150°C to + 150°C; dielectric permittivity of 10mol% Zr doped ceria as function of applied electric field and frequency; EDS-derived compositions for all ceramic samples; Off-equilibrium energy differences for MOx (M=Zr or Ce, x=7 or 8) or [Zr-Zr-Oy] (y= 13 or 14) displaced parallel to major crystallographic directions as calculated by DFT; Calculated Zr-O bond length distributions; Fourier transformed EXAFS spectra compared with AIMD-EXAFS simulations.

References

- 1. Newnham, R.; Sundar, V.; Yimnirun, R.; Su, J.; Zhang, Q., Electrostriction: nonlinear electromechanical coupling in solid dielectrics. The Journal of Physical Chemistry B 1997, 101, (48), 10141-10150.
- 2. Yavo, N.; Smith, A. D.; Yeheskel, O.; Cohen, S. R.; Korobko, R.; Wachtel, E.; Slater, P. R.; Lubomirsky, I., Large Nonclassical Electrostriction in (Y, Nb)-Stabilized delta-Bi2O3. Adv. Func. Mater. 2016, 26, (7), 1138-1142.
- 3. Uchino, K.; Cross, L. E., Electrostriction and Its Interrelation with Other Anharmonic Properties of Materials. Jpn. J. Appl. Phys. 1980, 19, (4), L171-L173.
- 4. Varenik, M.; Nino, J. C.; Wachtel, E.; Kim, S.; Yeheskel, O.; Yavo, N.; Lubomirsky, I., Dopant Concentration Controls Quasi-Static Electrostrictive Strain Response of Ceria Ceramics. ACS Appl. Mater. Interfaces 2020, 12, (35), 39381-39387.
- 5. Yavo, N.; Yeheskel, O.; Wachtel, E.; Ehre, D.; Frenkel, A. I.; Lubomirsky, I., Relaxation and saturation of electrostriction in 10 mol% Gd-doped ceria ceramics. Acta Mater. 2018, 144, 411-418.
- 6. Han, J.; Kabir, A.; Tinti, V. B.; Santucci, S.; Song, D. S.; Kim, S. Y.; Song, W.; Kim, E.; Bu, S. D.; Kern, F.; de Florio, D. Z.; Esposito, V., Enhanced electromechanical properties in low-temperature gadolinium-doped ceria composites with low-dimensional carbon allotropes. J. Mat. Chem. A 2022, 10, (8), 4024-4031.
- 7. Kabir, A.; Bowen, J. R.; Varenik, M.; Lubomirsky, I.; Esposito, V., Enhanced Electromechanical Response in Sm and Nd Co-doped Ceria. Materialia 2020, 12, 100728.
- 8. Kabir, A.; Tinti, V. B.; Varenik, M.; Lubomirsky, I.; Esposito, V., Electromechanical dopant–defect interaction in acceptor-doped ceria. Materials Advances 2020, 1, (8), 2717-2720.
- 9. Park, D. S.; Hadad, M.; Riemer, L. M.; Ignatans, R.; Spirito, D.; Esposito, V.; Tileli, V.; Gauquelin, N.; Chezganov, D.; Jannis, D.; Verbeeck, J.; Gorfman, S.; Pryds, N.; Muralt, P.; Damjanovic, D., Induced giant piezoelectricity in centrosymmetric oxides. Science 2022, 375, (6581), 653-657.
- 10. Santucci, S.; Zhang, H. W.; Kabir, A.; Marini, C.; Sanna, S.; Han, J. K.; Ulbrich, G.; Heppke, E. M.; Castelli, I. E.; Esposito, V., Electromechanically active pair dynamics in a Gddoped ceria single crystal. Phys Chem Chem Phys 2021, 23, (19), 11233-11239.
- 11. Tinti, V. B.; Kabir, A.; Han, J. K.; Molin, S.; Esposito, V., Gigantic electro-chemomechanical properties of nanostructured praseodymium doped ceria. Nanoscale 2021, 13, (16), 7583-7589.
- 12. Zhang, H. W.; Pryds, N.; Park, D. S.; Gauquelin, N.; Santucci, S.; Christensen, D. V.; Jannis, D.; Chezganov, D.; Rata, D. A.; Insinga, A. R.; Castelli, I. E.; Verbeeck, J.; Lubomirsky, I.; Muralt, P.; Damjanovic, D.; Esposito, V., Atomically engineered interfaces yield extraordinary electrostriction. Nature 2022, 609, (7928), 695-700.
- 13. Varenik, M.; Cohen, S.; Wachtel, E.; Frenkel, A. I.; Nino, J. C.; Lubomirsky, I., Oxygen vacancy ordering and viscoelastic mechanical properties of doped ceria ceramics. Scripta Mater. 2019, 163, 19-23.
- 14. Varenik, M.; Nino, J. C.; Wachtel, E.; Kim, S.; Cohen, S. R.; Lubomirsky, I., Trivalent Dopant Size Influences Electrostrictive Strain in Ceria Solid Solutions. ACS Appl. Mater. Interfaces 2021.

- 15. Korobko, R.; Lerner, A.; Li, Y. Y.; Wachtel, E.; Frenkel, A. I.; Lubomirsky, I., In-situ extended X-ray absorption fine structure study of electrostriction in Gd doped ceria. Appl. Phys. Lett. 2015, 106, (4), 042904.
- 16. Korobko, R.; Patlolla, A.; Kossoy, A.; Wachtel, E.; Tuller, H. L.; Frenkel, A. I.; Lubomirsky, I., Giant Electrostriction in Gd-Doped Ceria. Adv. Mater. 2012, 24, (43), 5857-5861.
- 17. Makagon, E.; Kraynis, O.; Merkle, R.; Maier, J.; Lubomirsky, I., Non-Classical Electrostriction in Hydrated Acceptor Doped BaZrO3: Proton Trapping and Dopant Size Effect. Adv. Func. Mater. 2021, 31, (50), Artn 2104188.
- 18. Kossoy, A.; Wang, Q.; Korobko, R.; Grover, V.; Feldman, Y.; Wachtel, E.; Tyagi, A. K.; Frenkel, A. I.; Lubomirsky, I., Evolution of the local structure at the phase transition in CeO₂-Gd₂O₃ solid solutions. Phys. Rev. B 2013, 87, (5), 1-4.
- 19. Li, Y.; Kraynis, O.; Kas, J.; Weng, T.-C.; Sokaras, D.; Zacharowicz, R.; Lubomirsky, I.; Frenkel, A. I., Geometry of electromechanically active structures in Gadolinium doped Cerium oxides. Aip Adv 2016, 6, (5), 055320.
- 20. Santucci, S.; Zhang, H.; Sanna, S.; Pryds, N.; Esposito, V., Electro-chemo-mechanical effect in Gd-doped ceria thin films with a controlled orientation. J. Mat. Chem. A 2020, 8, (28), 14023-14030.
- 21. Santucci, S.; Zhang, H. W.; Sanna, S.; Pryds, N.; Esposito, V., Electro-chemo-mechanical effect in Gd-doped ceria thin films with a controlled orientation. J. Mat. Chem. A 2020, 8, (28), 14023-14030.
- 22. Yu, J. C.; Janolin, P. E., Defining "giant" electrostriction. J. Appl. Phys. 2022, 131, (17), Artn 170701.
- 23. Zhang, H. W.; Vasiljevic, M.; Bergne, A.; Park, D. S.; Insinga, A. R.; Yun, S. H.; Esposito, V.; Pryds, N., Engineering of Electromechanical Oxides by Symmetry Breaking. Adv. Mater. Interfaces 2023, 10, (18).
- 24. Varenik, M.; Xu, B.; Li, J.; Gaver, E.; Wachtel, E.; Ehre, D.; Routh, P. K.; Khodorov, S.; Frenkel, A. I.; Qi, Y.; Lubomirsky, I., Lead-free Zr-doped ceria ceramics with low permittivity displaying giant electrostriction. Nat. Comm. 2023, 14, (1), 7371.
- 25. Review of Electrostrictive Materials. In *Fundamentals of Smart Materials*, Shahinpoor, M., Ed. 2020; p 36.
- 26. Uchino, K., Relaxor Ferroelectric-Based Ceramics. In *Woodh Pub Ser Elect*, 2017; pp 127-153.
- 27. Uchino, K., Electrostrictive and Piezoelectric Effects in Relaxor Ferroelectrics: Historical Background. Ieee Transactions on Ultrasonics Ferroelectrics and Frequency Control 2022, 69, (11), 3013-3036.
- 28. Nomura, S.; Tonooka, K.; Kuwata, J.; Cross, L. E.; Newnham, R. E., Electrostriction in Pb(Mg1/3nb2/3)O3 Ceramics. Ferroelectrics 1980, 29, (1-2), 124-124.
- 29. Kraynis, O.; Timoshenko, J.; Huang, J.; Singh, H.; Wachtel, E.; Frenkel, A. I.; Lubomirsky, I., Modeling Strain Distribution at the Atomic Level in Doped Ceria Films with Extended X-ray Absorption Fine Structure Spectroscopy. Inorg. Chem. 2019, 58, (11), 7527-7536.
- 30. Yavo, N.; Nissenbaum, A.; Wachtel, E.; Shaul, T. E.; Mendelson, O.; Kimmel, G.; Kim, S.; Lubomirsky, I.; Yeheskel, O., Rapid sintering protocol produces dense ceria-based ceramics. J. Am. Ceram. Soc. 2018, 101, (11), 4968-4975.
- 31. ZrO₂, N. C.-. NIST phase digrams database, entry #3630; https://phaseonline-ceramics-org. In.

- 32. Yavo, N.; Noiman, D.; Wachtel, E.; Kim, S.; Feldman, Y.; Lubomirsky, I.; Yeheskel, O., Elastic moduli of pure and gadolinium doped ceria revisited: sound velocity measurements. Scripta Mater. 2016, 123, 86-89.
- 33. Ravel, B.; Newville, M., ATHENA, ARTEMIS, HEPHAESTUS: data analysis for X-ray absorption spectroscopy using IFEFFIT. J. Synchrotron Rad. 2005, 12, (4), 537-541.
- 34. Perdew, J. P.; Burke, K.; Ernzerhof, M., Generalized gradient approximation made simple. Phys. Rev. Lett. 1996, 77, (18), 3865-3868.
- 35. Dudarev, S. L.; Botton, G. A.; Savrasov, S. Y.; Humphreys, C. J.; Sutton, A. P., Electron-energy-loss spectra and the structural stability of nickel oxide: An LSDA+U study. Phys. Rev. B 1998, 57, (3), 1505-1509.
- 36. Fabris, S.; de Gironcoli, S.; Baroni, S.; Vicario, G.; Balducci, G., Taming multiple valency with density functionals: A case study of defective ceria. Phys. Rev. B 2005, 71, (4), 041102.
- 37. Chiang, H.-W.; Blumenthal, R. N.; Fournelle, R. A., A high temperature lattice parameter and dilatometer study of the defect structure of nonstoichiometric cerium dioxide. Sol. State Ionics 1993, 66, (1), 85-95.
- 38. Kresse, G.; Joubert, D., From ultrasoft pseudopotentials to the projector augmented-wave method. Phys. Rev. B 1999, 59, (3), 1758-1775.
- 39. Das, T.; Nicholas, J. D.; Sheldon, B. W.; Qi, Y., Anisotropic chemical strain in cubic ceria due to oxygen-vacancy-induced elastic dipoles. Phys Chem Chem Phys 2018, 20, (22), 15293-15299.
- 40. Stukowski, A., Visualization and analysis of atomistic simulation data with OVITO-the Open Visualization Tool. Modelling and Simulation in Materials Science and Engineering 2010, 18, (1), Artn 015012.
- 41. Kas, J. J.; Vila, F. D.; Pemmaraju, C. D.; Tan, T. S.; Rehr, J. J., Advanced calculations of X-ray spectroscopies with FEFF10 and Corvus. J. Synchrotron Rad. 2021, 28, (6), 1801-1810.
- 42. Newville, M., Larch: An Analysis Package for XAFS and Related Spectroscopies. 15th International Conference on X-Ray Absorption Fine Structure (Xafs15) 2013, 430.
- 43. Ravel, B.; Newville, M., :: data analysis for X-ray absorption spectroscopy using. J. Synchrotron Rad. 2005, 12, 537-541.
- 44. Mendelson, M. I., Average grain size in polycrystalline ceramics. J. Am. Ceram. Soc. 1969, 52, (8), 443-446.
- 45. Ledbetter, H. M.; Datta, S. K., Effective Wave Speeds in an Sic-Particle-Reinforced Al Composite. J Acoust Soc Am 1986, 79, (2), 239-248.
- 46. Ledbetter, H. M.; Austin, M. W.; Kim, S. A.; Lei, M., Elastic constants and Debye temperature of polycrystalline Y1Ba2Cu3O7–x. J. Mater. Res. 2011, 2, (6), 786-789.
- 47. Koettgen, J.; Duck, G.; Martin, M., The oxygen ion conductivity of Lu doped ceria. J. Physics 2020, 32, (26), 265402.
- 48. Koettgen, J.; Grieshammer, S.; Duck, G.; Ulbrich, G.; Lerch, M.; Martin, M., Ab initio and experimental oxygen ion conductivities in Sm-Zr and Gd-Zr co-doped ceria. Sol. State Ionics 2020, 355, Artn 115422.
- 49. Koettgen, J.; Grieshammer, S.; Hein, P.; Grope, B. O. H.; Nakayama, M.; Martin, M., Understanding the ionic conductivity maximum in doped ceria: trapping and blocking. Phys Chem Chem Phys 2018, 20, (21), 14291-14321.
- 50. Stevanovic, V.; Lany, S.; Zhang, X. W.; Zunger, A., Correcting density functional theory for accurate predictions of compound enthalpies of formation: Fitted elemental-phase reference energies. Phys. Rev. B 2012, 85, (11), Artn 115104.

- 51. Palmer, B. J.; Pfund, D. M.; Fulton, J. L., Direct modeling of EXAFS spectra from molecular dynamics simulations. J. Phys. Chem. 1996, 100, (32), 13393-13398.
- 52. DAngelo, P.; DiNola, A.; Mangoni, M.; Pavel, N. V., An extended x-ray absorption fine structure study by employing molecular dynamics simulations: Bromide ion in methanolic solution. J Chem Phys 1996, 104, (5), 1779-1790.
- 53. Roscioni, O. M.; Zonias, N.; Price, S. W. T.; Russell, A. E.; Comaschi, T.; Skylaris, C. K., Computational prediction of EXAFS spectra of gold nanoparticles from classical molecular dynamics simulations. Phys. Rev. B 2011, 83, (11), Artn 115409.
- 54. Timoshenko, J.; Duan, Z.; Henkelman, G.; Crooks, R. M.; Frenkel, A. I., Solving the Structure and Dynamics of Metal Nanoparticles by Combining X-Ray Absorption Fine Structure Spectroscopy and Atomistic Structure Simulations. Annual Review of Analytical Chemistry, Vol 12 2019, 12, (1), 501-522.
- 55. Owen, C. J.; Marcella, N.; Xie, Y.; Vandermause, J.; I., F. A.; Nuzzo, R. G.; Kozinsky, B., Unraveling the Catalytic Effect of Hydrogen Adsorption on Pt Nanoparticle Shape-Change. In 2306.00901, Ed. arXiv: 2023.

TOC graphics

